Green Chemistry

PAPER

View Article Online
View Journal

Cite this: DOI: 10.1039/d6gc00981f

Revealing sulfur-resistant Pt–CeO_2 interfacial sites for water–gas shift catalysts toward waste-to-hydrogen

Ga-Ram Hong, Kyoung-Jin Kim, Bong-Gyeong Shin and Hyun-Seog Roh *

The effects of introducing various transition (Nb, Mo, W, and Re) and nontransition (Al, Ga, Sn, and Pb) metal promoters into Pt/CeO_2 catalysts on sulfur tolerance, catalytic activity, and regeneration behavior during waste-to-hydrogen conversion processes were investigated. Although the impact of promoter addition depended on the metal species, all promoters interacted with both the active metal and the CeO_2 support, inducing interfacial reorganization and generating additional oxygen defects, thereby enhancing the oxygen storage capacity of the Pt/CeO_2 catalysts. Mobile oxygen species present on the catalyst surface can react with sulfur species adsorbed at active sites, facilitating their oxidation and desorption and contributing to catalytic regeneration. Catalytic evaluations revealed that only transition metal-doped Pt/CeO_2 catalysts maintained enhanced oxygen mobility under sulfur-containing conditions through strong Pt–O–Ce interfacial interactions, resulting in a significant improvement in sulfur tolerance and activity regeneration performance compared with the unpromoted Pt/CeO_2 catalyst. These findings demonstrate that preserving a Pt–O–Ce interfacial structure under sulfur exposure is an additional and previously underappreciated requirement for achieving sulfur tolerance. This insight provides a foundation for the development of highly durable catalyst systems applicable to waste-to-hydrogen technologies.

Received 13th February 2026,
Accepted 10th April 2026

DOI: 10.1039/d6gc00981f

rsc.li/greenchem

Green foundation

1. Hydrogen production from municipal solid waste *via* the water–gas shift reaction is a sustainable solution for a future hydrogen economy. However, waste-derived synthesis gas presents critical challenges, including high CO concentrations, composition fluctuations due to diverse feedstock components, and catalyst deactivation caused by sulfur impurities. This work proposes a durable catalyst design strategy for efficient waste-to-hydrogen conversion.
2. The Nb- and W-promoted Pt/CeO_2 catalysts achieved up to 93% of the equilibrium CO conversion under sulfur-free conditions with waste-derived synthesis gas. The catalysts maintained over 60% CO conversion under continuous exposure to 1000 ppm H_2S and recovered most of their initial activity after sulfur injection was stopped. More importantly, this study identified the catalytic characteristics responsible for high sulfur tolerance.
3. Future research should focus on maintaining durability and sulfur tolerance at lower operating temperatures for on-site industrial system applications.

1. Introduction

As the transition toward carbon-neutral energy systems accelerates, global interest in hydrogen as a clean energy carrier capable of replacing fossil fuels has steadily increased.[1] In this context, growing attention has been directed toward waste-to-hydrogen technologies, one of the waste-to-energy approaches, as sustainable resource-circulating energy systems that can simultaneously address increasing waste management challenges and rising energy demand.[1–3] Conventional waste-to-energy technologies typically involve the incineration of waste to generate heat and electricity.[4] However, with the introduction of advanced thermochemical processes such as gasification and pyrolysis, waste can be converted into fundamental chemical building blocks (CO, H_2, or hydrocarbons) rather than being burned, enabling the production of value-added materials and clean fuels such as hydrogen.[3,5] Among these approaches, gasification enables the conversion of municipal solid waste into synthesis gas primarily comprising CO and H_2.[2,6] Such waste-to-hydrogen processes aim to convert waste-derived synthesis gas into hydrogen-rich streams through downstream catalytic reactions, supporting efficient resource utilization. To enable the use of hydrogen from waste in fuel cell applications, CO removal is essential, while controlling the H_2/CO ratio is also required for downstream synthesis of value-added materials. Given these requirements, the water–gas shift (WGS, $CO + H_2O \leftrightarrow H_2 + CO_2$) reaction plays a key role by con-

Department of Environmental and Energy Engineering, Yonsei University, 1 Yonseidae-gil, Wonju, Gangwon 26493, Republic of Korea.
E-mail: hsroh@yonsei.ac.kr

verting CO into CO_2 while producing additional hydrogen.[7,8] However, waste-derived synthesis gas exhibits fluctuations in composition due to feedstock heterogeneity and contains substantially higher CO concentrations (up to ~40%) and impurities (*e.g.*, sulfur species, <0.1%) than synthesis gas from natural gas reforming (~10% CO), which act as catalyst poisons that severely inhibit WGS activity and compromise the stability of sustainable hydrogen production.[2,6,9] Accordingly, the development of impurity-tolerant WGS catalysts is essential for ensuring stable and sustainable hydrogen production from waste-derived resources.

Pt/CeO_2-based catalysts have been studied for the WGS reaction owing to their high intrinsic activity, as the redox properties of ceria and the metal–support interaction (MSI) at the Pt–CeO_2 interface enhance oxygen mobility and promote the Mars-van Krevelen mechanism.[10–12] CeO_2-based materials exhibit high oxygen storage capacity (OSC) arising from reversible Ce^{3+}/Ce^{4+} redox transitions, which is known to enhance WGS activity by facilitating H_2O dissociation and redox cycling.[13] Previous studies have shown that highly dispersed Pt active sites supported on CeO_2 with high OSC can promote the oxidation and removal of adsorbed sulfur species by mobile oxygen, thereby mitigating sulfur-induced catalyst deactivation.[14–19]

The rational modulation of the metal–support interface through promoter addition represents an effective strategy for simultaneously controlling oxygen vacancy formation and electronic interactions. Metal promoters can function as textural, structural, or guard promoters, thereby regulating metal–oxygen bond strength, surface hydroxyl concentration, and the number of accessible active sites. However, certain metal dopants can instead deteriorate catalytic activity, highlighting the importance of understanding the intrinsic properties of the constituent materials and their mutual interactions. Transition metals can serve as additives to regulate the metal–support interfacial structure and catalytic performance.[20–25] For instance, the addition of niobium to CeO_2-based catalysts substitutes Ce^{4+} with Nb^{5+}, thereby promoting electron excitation, which modifies the electron density at the metal–support interface.[20,21] Molybdenum addition to Pt catalysts forms interfacial active sites favorable for water activation at the interface between Pt and Mo species.[22] Wang *et al.* demonstrated that tungsten acts as an effective electronic and structural promoter, enabling fine tuning of the local environment of Pt.[23] Rhenium has been reported to improve catalyst stability and activity by preventing Pt nanoparticle sintering and providing additional pathways for water activation and oxygen/hydroxyl transfer.[24,25] Conversely, non-transition metals can also serve as additives to induce oxygen defects or enhance the structural stability of the catalyst.[26–31] Aluminum is widely used as a support in WGS reactions because it provides Lewis acid sites to promote water dissociation while increasing catalyst surface area and thermal stability.[26] Vecchietti *et al.* reported that the introduction of gallium into Pt/CeO_2-based catalysts can efficiently control oxygen vacancies within the support.[27] Tin possesses reversible redox behavior (Sn^{4+}/Sn^{2+}), similar to CeO_2, allowing modulation of the electronic structure when combined with the CeO_2 support.[28,29] Lastly, lead deposited on the catalyst surface as an additive can secure reaction catalytic selectivity and stability by regulating the active sites.[30,31] The general relationship between the characteristics of metal dopants and their influence on sulfur resistance in platinum-based catalysts remains unclear. A systematic understanding of this relationship is essential for the rational selection of promoters in the design of sulfur-tolerant WGS catalysts.

In this study, various transition and nontransition metal promoters were introduced to Pt/CeO_2-based WGS catalysts to enhance sulfur tolerance and regeneration behavior under waste-derived synthesis gas. Furthermore, this work systematically investigates the *in situ* regeneration capabilities of these catalysts, aiming to extend their lifespans without relying on chemical reactivation processes or frequent catalyst disposal. Despite their practical importance, the durability and regeneration characteristics of Pt/CeO_2-based catalysts under sulfur-containing WGS conditions relevant to waste-derived synthesis gas remain insufficiently understood. Therefore, this work systematically compares promoter effects under identical preparation and reaction conditions, and the catalysts were evaluated under harsh WGS conditions, including reactant compositions simulating actual gasification-derived synthesis gas, high gas hourly space velocities, and H_2S concentrations exceeding 1000 ppm. This study provides mechanistic insights into promoter-dependent structure–performance relationships and presents design guidelines for durable Pt/CeO_2-based WGS catalysts suitable for waste-derived synthesis gas applications.

2. Experimental

2.1. Synthesis of supports and catalysts

2.1.1. Synthesis of the CeO_2 support. The CeO_2 support was prepared by a precipitation method. Cerium nitrate hexahydrate ($Ce(NO_3)_3{\cdot}6H_2O$, 99%; Sigma-Aldrich) was dissolved in 500 mL of distilled water and then heated to 80 °C under continuous stirring. When the Ce precursor solution reached 80 °C, 15% KOH (95%; Samchun Chemicals) was added at a rate of 50 mL min^{-1} in a stoichiometric amount as a precipitating agent. After digestion for 72 h at 80 °C, the resulting precipitate was cooled to room temperature and purified by five sequential washings with distilled water to eliminate residual impurities. The washed precipitate was then oven dried at 100 °C for 12 h, followed by calcination in a furnace at 500 °C for 6 h to yield CeO_2 powder.

2.1.2. Synthesis of the Pt/CeO_2 catalyst. The Pt/CeO_2 catalysts were prepared by impregnating Pt onto the as-prepared CeO_2 support using the incipient wetness impregnation method, with the Pt loading fixed at 1 wt%. Tetraammineplatinum(II) nitrate ($[Pt(NH_3)_4](NO_3)_2$, 50% Pt basis; Sigma-Aldrich) was dissolved in distilled water and deposited dropwise onto the CeO_2 support. The impregnated samples were dried at 100 °C for 12 h and subsequently calcined at 500 °C for 6 h.

2.1.3. Synthesis of Me/Pt/CeO_2 catalysts. Promoter metals were introduced onto the pre-synthesized Pt/CeO_2 catalyst using the incipient wetness impregnation method. Transition metals (Nb, W, Mo, and Re) and nontransition metals (Al, Sn, Ga, and Pb) were employed as promoters, and the promoter loading was fixed at 2 wt% for all samples. Stoichiometric amounts of niobium(v) oxalate hydrate ($Nb(HC_2O_4)_5{\cdot}xH_2O$, 19.9% Nb_2O_5; Alfa Aesar), ammonium molybdate tetrahydrate ($(NH_4)_6Mo_7O_{24}{\cdot}4H_2O$, 99%; Sigma-Aldrich), ammonium metatungstate hydrate ($(NH_4)_6H_2W_{12}O_{40}{\cdot}xH_2O$, 99.99%; Sigma-Aldrich), ammonium perrhenate (NH_4ReO_4, 99%; Sigma-Aldrich), aluminum nitrate nonahydrate ($Al(NO_3)_3{\cdot}9H_2O$, 98%; Sigma-Aldrich), gallium(III) nitrate hydrate ($Ga(NO_3)_3{\cdot}xH_2O$, 99; Sigma-Aldrich), tin(IV) chloride pentahydrate ($SnCl_4{\cdot}5H_2O$, 98%; Daejung), and lead(II) nitrate ($Pb(NO_3)_2$, 99.999%; Sigma-Aldrich) were dissolved in distilled water and used as precursor solutions for impregnation. The resulting samples were oven dried at 100 °C for 12 h and subsequently calcined at 500 °C for 6 h. The final catalysts were designated as Me/Pt/CeO_2 (Me = Nb, Mo, W, Re, Al, Ga, Sn and Pb).

2.1.4. Synthesis of Me/CeO_2 samples. To examine the effect of the promoter metals in the absence of Pt, CeO_2-supported promoter-only catalysts were prepared. The promoter loading was fixed at 2 wt%. The same promoter precursors described in section 2.1.3 were used, and the preparation procedure, including impregnation, drying, and calcination, was identical to that described in section 2.1.2. These samples are denoted as Me/CeO_2.

2.2. Characterization

The physicochemical properties of the support and all catalysts were investigated by X-ray diffraction (XRD) patterns, Brunauer–Emmett–Teller (BET) analysis, pulsed CO-chemisorption, H_2-temperature-programmed reduction (H_2-TPR), Raman spectroscopy, X-ray photoelectron spectroscopy (XPS), H_2–O_2 pulse chemisorption, and *in situ* CO diffuse reflectance infrared Fourier transform spectroscopy (CO-DRIFTS). The detailed characterization procedures are described in the SI.

2.3. Catalytic evaluation

The catalytic activity for the WGS reaction was evaluated in a fixed-bed quartz reactor (4 mm inner diameter) placed inside a furnace. Quartz wool was used as a support layer, and catalysts were loaded on top of this for the reaction. A K-type thermocouple was positioned at the catalyst bed to directly monitor the catalyst temperature. Before the reaction, the catalyst samples were reduced *in situ* at 400 °C for 1 h under the flow of a 5% H_2/N_2 gas mixture at ambient pressure. The reaction was performed using a feed gas mixture simulating the composition of waste-derived synthesis gas from a municipal solid waste gasifier.[32] The premixed gas (CO: 38.4 vol%, H_2: 28.6 vol%, CO_2: 21.8 vol%, N_2: 8.9 vol%, and CH_4: 2.3 vol%, Kyungwon Oxygen Co., Ltd) and steam were introduced into the reactor through mass-flow controllers and a syringe pump, respectively. Water vapor was preheated to 180 °C using a heating coil before injection. The steam-to-carbon ratio was maintained at 2.0. The catalytic activity test was conducted at temperatures ranging from 350 to 500 °C in 50 °C intervals under a gas hourly space velocity (GHSV) of 46 000 h^{-1}. To evaluate the sulfur resistance of the catalysts, sulfur tolerance tests were conducted at 400 °C by continuously introducing H_2S at a concentration of 1000 ppm into the feed gas for 12 h. Subsequently, to assess the long-term stability and regeneration behavior under more severe sulfur conditions, the H_2S concentration was increased to 1500 ppm, and a 4-cycle sulfur on/off switching test was performed by alternately supplying and cutting off H_2S while monitoring the catalytic activity and regeneration capability. After removal of residual H_2O and sulfur-containing species in the outlet line, the product gas was analyzed using online micro-gas chromatography (Micro GC Fusion, Inficon). The gas analysis system was equipped with two columns. Column A utilized a 10 m Rt-Molsieve 5A column operated at 90 °C and 20 psig with a thermal conductivity detector (TCD) and Ar carrier gas to detect H_2, N_2, CH_4, and CO. Column B utilized a 12 m Rt-Q-Bond column operated at 60 °C and 20 psig with a TCD and He carrier gas to detect CO_2. All components were quantified following calibration with standard gas mixtures, and the peak areas were converted to mole fractions using component-specific response factors. The CO conversion, CO_2 selectivity and CH_4 selectivity were determined according to the following equations:

$$\text{CO conversion}\ (\%) = \frac{[CO]_{in} - [CO]_{out}}{[CO]_{in}} \times 100 \quad (1)$$

$$CO_2\ \text{selectivity}\ (\%) = \frac{[CO_2]_{out} - [CO_2]_{in}}{\left([CH_4]_{out} - [CH_4]_{in}\right) + \left([CO_2]_{out} - [CO_2]_{in}\right)} \times 100 \quad (2)$$

$$CH_4\ \text{selectivity}\ (\%) = \frac{[CH_4]_{out} - [CH_4]_{in}}{\left([CH_4]_{out} - [CH_4]_{in}\right) + \left([CO_2]_{out} - [CO_2]_{in}\right)} \times 100 \quad (3)$$

3. Results and discussion

3.1. Catalytic performance in the WGS reaction

Pt/Ce catalysts doped with various transition and nontransition metals were applied to the WGS reaction using waste-derived synthesis gas. The WGS performance of all prepared catalysts, evaluated in the temperature range of 350–500 °C, is shown in Fig. S1. The unpromoted Pt/Ce catalyst exhibited a high CO conversion of >85% across the entire temperature range (350–500 °C). The incorporation of Nb, W, Al, and Ga not only preserved the originally high CO conversion of the Pt/Ce catalyst but also led to enhancements at specific temperatures. In contrast, several other metals (Mo, Re, Sn, and Pb) led to lower CO conversion of the catalyst, indicating that promoter effects depend on the chemical properties of the added metals. Fig. 1(A) shows the catalytic performance of the representative Me/Pt/Ce catalysts (Me = Nb, W, Al, and Ga) with

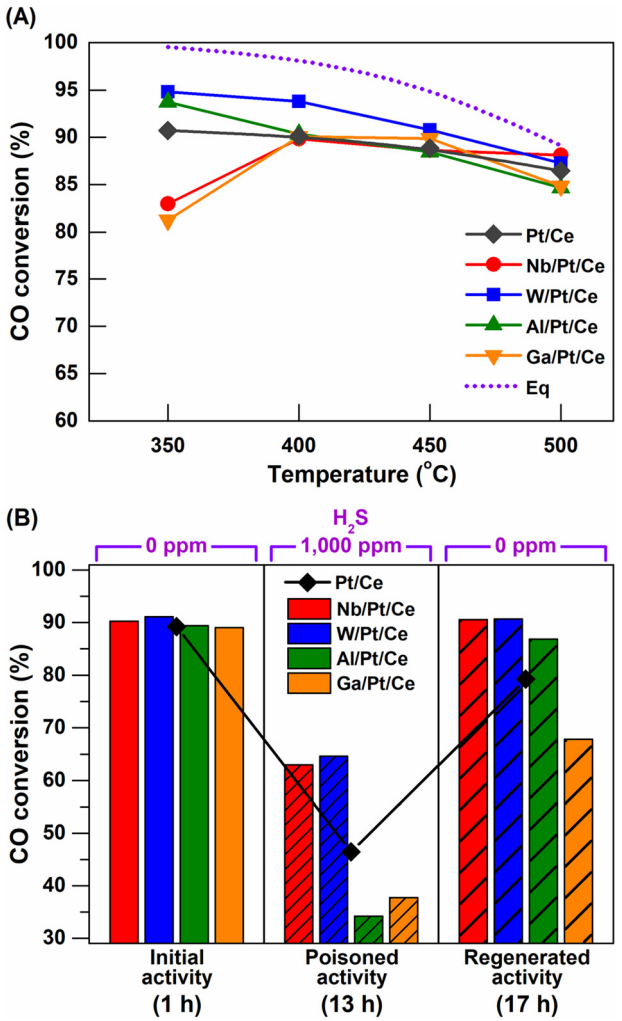

Fig. 1 Catalytic performance of Pt/Ce catalysts with various metal promoters. (A) CO conversion as a function of temperature; (B) CO conversion as a function of time following the injection of 1000 ppm H_2S at 400 °C. Reaction conditions: $H_2O/(CH_4 + CO + CO_2)$ = 2.0; GHSV = 46 000 mL g^{-1} h^{-1}.

these selected metal promoters. All selected catalysts exhibited excellent CO conversions approaching the equilibrium over the entire reaction temperature range (350–500 °C), as shown in Fig. 1(A). No side reactions, particularly CO methanation ($CO + 3H_2 \rightarrow CH_4 + H_2O$), were observed for any of the catalysts (Fig. S2).

To consider the presence of sulfur impurities in waste-derived feed gas, the selected catalysts were evaluated under sulfur-containing reaction conditions.[2] Sulfur is known to act as a strong poison for most metal catalysts, leading to rapid deactivation.[2,9,33] The sulfur tolerance of the Me/Pt/Ce catalysts was examined at 400 °C in three stages, as illustrated in Fig. 1(B): (i) initial activity test (0–1 h), confirmation of the baseline WGS performance under sulfur-free conditions; (ii) sulfur-tolerance test (1–13 h), evaluation of the catalytic activity under continuous injection of 1000 ppm H_2S for 12 h; and (iii) catalytic activity-regeneration test (13–17 h), observation of the recovery behavior after sulfur injection was stopped. The CO conversion values shown in Fig. 1(B) correspond to representative data points measured at the end of each stage after 1, 13, and 17 h. These three stages were performed continuously for a total of 17 h, and the time-dependent changes in CO conversion are shown in Fig. S3. All catalysts showed high CO conversion rates of more than 90% under initial conditions, consistent with the results shown in Fig. 1(A). However, after introducing 1000 ppm H_2S, all Pt/Ce-based catalysts underwent rapid deactivation. The Nb- and W-promoted catalysts maintained CO conversion rates above 60%, which were ~15% higher than the unpromoted Pt/Ce catalyst. In comparison, the Al- and Ga-promoted catalysts showed a decrease in CO conversion to about 40%. After stopping the sulfur injection under continuous reactant flow, all catalysts exhibited a recovery trend in CO conversion. It has been reported that the desorption of sulfur species accelerates significantly at around 300 °C.[34,35] Given that the reaction temperature in this study (400 °C) is sufficiently high, stopping the sulfur feed promotes sulfur desorption. Under sulfur-free conditions, the adsorbed sulfur can react with spillover oxygen, H_2, and CO in the feed stream and gradually desorb from the active sites, leading to the recovery of catalytic activity. Notably, the Nb- and W-added catalysts recovered most of their initial catalytic activity, demonstrating excellent sulfur resistance and regeneration ability. Although the Al-promoted catalyst exhibited the most severe deactivation upon sulfur poisoning, it recovered over 90% of its original CO conversion, showing a higher regeneration rate than the Pt/Ce catalyst. In contrast, the Ga-promoted catalyst showed the lowest regeneration rate among all catalysts, with the recovered CO conversion remaining below 70%, indicating substantially diminished catalytic activity. Additionally, no side reactions were observed in any of the catalysts (Fig. S4).

3.2. Structural and redox properties of promoted Pt/Ce catalysts

Fig. 2(A) shows the XRD patterns of all the prepared CeO_2 supports and Me/Pt/Ce catalysts. All catalysts exhibited the fluorite cubic structure of cerium oxide (PDF-ICDD #34-0394), and no diffraction peaks corresponding to Pt and promoter (Nb, W, Al, and Ga)-related species were observed. This can be attributed to the relatively low metal loadings, with Pt and the promoter metals present at 1 wt% and 2 wt%, respectively. In addition, this behavior may be associated with the partial incorporation of Pt and promoter metals into the ceria lattice, since the ionic radii of Pt (Pt^{4+} = 0.63 Å and Pt^{2+} = 0.80 Å), W^{6+} (0.60 Å), Nb^{5+} (0.64 Å), Al^{3+} (0.54 Å), and Ga^{3+} (0.62 Å) are smaller than that of ceria lattice cations (Ce^{4+} = 0.97 Å and Ce^{3+} = 1.28 Å).[36–40] Therefore, the absence of Pt- and promoter-related diffraction peaks is attributed to one or a combination of the following factors, including low metal contents, partial incorporation of the metal species into the ceria lattice, and high dispersion as nanosized or amorphous species below the XRD detection limit.

The specific surface areas of the CeO_2 support and the Me/Pt/Ce catalyst are summarized in Table 1. The CeO_2 support exhibited a BET surface area of 161 m^2 g^{-1}. All the prepared

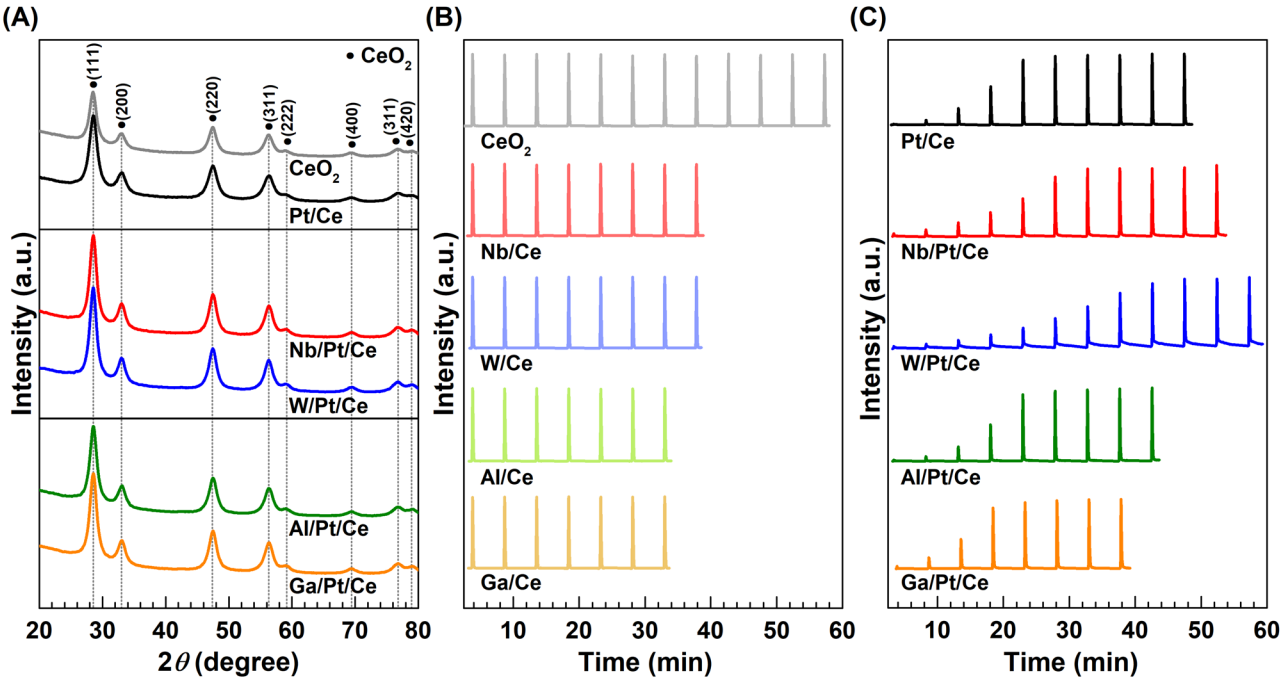

Fig. 2 (A) XRD patterns of the reduced CeO_2 support and Pt/Ce catalysts with various metal promoters. Pulsed CO-chemisorption curves of (B) the Me/Ce samples and (C) Me/Pt/Ce catalysts with various metal promoters.

Table 1 Physicochemical properties of the CeO_2 support and Pt/Ce catalysts with various metal promoters

Catalyst	Surface area[a] ($m^2\ g^{-1}$)	Pore volume[a] ($cm^3\ g^{-1}$)	Pt dispersion[b] (%)
CeO_2	161	0.418	—
Pt/Ce	124	0.385	104
Nb/Pt/Ce	106	0.263	129
W/Pt/Ce	112	0.340	156
Al/Pt/Ce	93	0.276	101
Ga/Pt/Ce	107	0.309	82

[a] Estimated from N_2 adsorption at −196 °C. [b] Estimated from pulsed CO-chemisorption.

catalysts exhibited a lower specific surface area than that of the CeO_2 support because they underwent a subsequent high-temperature calcination step after the active metal was loaded onto the support. Specifically, after the preparation of the CeO_2 support, Pt was impregnated and calcined to form the Pt/Ce catalyst, followed by promoter impregnation and a subsequent calcination step to obtain the Me/Pt/Ce catalysts. Compared with the Pt/Ce catalyst containing only 1 wt% Pt, the Me/Pt/Ce catalysts with an additional 2 wt% promoter exhibited a more pronounced decrease in specific surface area. Among these, the W/Pt/Ce catalyst maintained the highest specific surface area, whereas the Al-promoted Pt/Ce catalyst showed the largest decrease. All catalysts exhibited type IV adsorption–desorption isotherms with hysteresis loops in the P/P_0 range of 0.7–1.0 (Fig. S5), indicating the presence of mesopores between particles.[41]

Table 1 lists the Pt dispersion values calculated from pulsed CO-chemisorption measurements. The Pt dispersion was calculated assuming a 1 : 1 stoichiometric adsorption of CO on surface-exposed Pt atoms. The calculated Pt dispersions exceeded 100% for most catalysts, indicating that the actual dispersion was overestimated. The excessive CO uptake commonly observed in noble metal catalysts supported on cerium-based oxides is associated with the redox property of CeO_2.[42–44] In particular, CO adsorbed at Pt active sites can react with mobile surface oxygen of CeO_2 *via* oxygen reverse spillover, leading to an apparent overestimation of the Pt dispersion.[42,45] To further clarify the contributions of the CeO_2 support and the promoters to this overestimation, Me/CeO_2 samples were prepared and subjected to pulsed CO-chemisorption measurements. Fig. 2(B and C) presents the CO pulse profiles of the CeO_2 support, Me/CeO_2 samples, and Me/Pt/CeO_2 catalysts as a function of time. The CeO_2 support reached adsorption saturation after the very first CO pulse, confirming that CeO_2 alone scarcely adsorbs CO at 50 °C (Fig. 2(B)). Similarly, all Me/CeO_2 samples exhibited negligible CO uptake. In contrast, as shown in Fig. 2(C), clear CO adsorption signals were observed for both Pt/CeO_2 and Me/Pt/CeO_2 catalysts, demonstrating that CO adsorption occurs primarily in the presence of Pt active sites. In terms of calculated Pt dispersion, W/Pt/Ce exhibited the highest value (156%), followed by Nb/Pt/Ce (129%), Pt/Ce (104%), Al/Pt/Ce (101%), and Ga/Pt/Ce (82%). The W- and Nb-promoted catalysts demonstrated significantly enhanced dispersion relative to the Pt/Ce catalyst, whereas the Al- and Ga-promoted catalysts exhibited decreased dispersion, with the Ga/Pt/Ce catalyst showing the lowest value.

Accordingly, the observed differences in CO uptake among catalysts with identical Pt loadings indicate promoter-induced variations in the nature and extent of Pt–CeO_2 interfacial interactions. In the Pt–CeO_2 system, strong MSIs promote the formation of Pt–O–Ce species, which facilitate rapid electron transfer and lattice oxygen migration between the surface and the bulk.[43,46] CO adsorbed on Pt can, through activated Pt–O–Ce interfacial sites, further react with CeO_2 surface oxygen during CO-chemisorption measurements, leading to an apparent overestimation of Pt dispersion.[45] Pt dispersions exceeding 100% do not accurately represent the true geometric dispersion of Pt, but rather serve as an indirect indicator of the reactivity of Pt–O–Ce interfacial sites that activate lattice oxygen. Since catalytic reaction occurs on the catalyst surface, dispersion is one of the key factors affecting catalytic activity. Indeed, the results of the sulfur-resistance tests shown in Fig. 1(B) exhibited a similar trend to that of Pt dispersion. The Nb/Pt/Ce and W/Pt/Ce catalysts, which showed higher dispersion than that of the Pt/Ce catalyst, maintained high CO conversion levels even under sulfur-injected reaction conditions. Conversely, the Al/Pt/Ce and Ga/Pt/Ce catalysts, with relatively low dispersion, showed lower activity than that of the Pt/Ce catalyst after H_2S injection. Overall, these results indicate that promoter-modified Pt–CeO_2 interfacial interactions not only influence CO adsorption behavior but also contribute to maintaining catalytic activity under sulfur-poisoned conditions.

The reduction properties of the catalyst were investigated using H_2-TPR analysis. As shown in Fig. 3(A), the CeO_2 support exhibited two reduction peaks divided into a broad peak around 500 °C and a high-temperature peak above 700 °C. The first peak corresponds to the reduction of CeO_2 surface oxygen, and the second peak corresponds to the reduction of bulk CeO_2.[13,47] For the Pt/Ce catalyst, in which Pt is supported on a CeO_2 support, a distinct reduction peak appeared around 200 °C, accompanied by a significant decrease in the reduction peak of the CeO_2 surface. This behavior indicates that Pt doping promotes the reduction of CeO_2 surface oxygen *via* oxygen reverse spillover, mediated by strong Pt–CeO_2 interfacial interactions, which is consistent with the pulsed CO-chemisorption results.[45,47] The low-temperature peak of the CeO_2-based Pt catalyst is assigned to the reduction of PtO_x on the surface, Pt species bonded to Ce through Pt–O–Ce bonds, and surface oxygen on CeO_2.[48–50]

Fig. 3(B) shows that a main reduction peak was also observed around 100–200 °C for all Me/Pt/Ce catalysts, with a diminished surface reduction peak of CeO_2. In general, the stronger the MSI, the higher the temperature at which the reduction peak appears.[47–49] Compared with the Pt/Ce catalyst, all promoter-added Pt/Ce catalysts showed reduction peaks at lower temperatures. This downward shift of the low-temperature peak suggests that the Pt–Ce interaction was relatively weakened upon promoter introduction. In contrast, the unpromoted Pt/Ce catalyst, lacking promoter effects, exhibits the strongest Pt–O–Ce bonding among the prepared catalysts. The Nb/Pt/Ce and W/Pt/Ce catalysts exhibited a strong peak at 206 °C, confirming that the Pt–CeO_2 interfacial interaction was largely maintained. The Al/Pt/Ce and Ga/Pt/Ce catalysts showed main reduction peaks around 160 °C and 128 °C, respectively. In particular, the Al- and Ga-modified catalysts exhibit two or more weakly separated reduction peaks. This indicates a relative weakening of the MSI, leading to the sequential reduction of weakly bound Pt species and relatively strongly bound Pt–O–Ce species on the CeO_2 surface at lower temperatures.[47,48] To confirm the effect of the promoters, Me/CeO_2 samples without Pt were examined (Fig. 3(C)). When a promoter was introduced, a tendency for the CeO_2 surface reduction peak to shift to lower temperatures was observed.

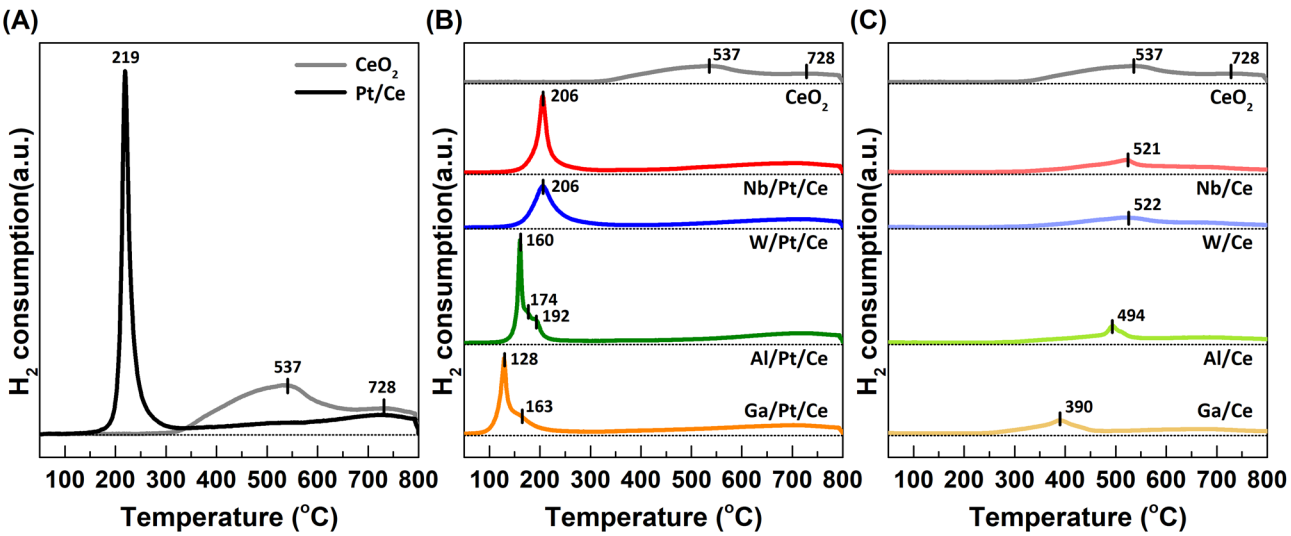

Fig. 3 H_2-TPR profiles of the CeO_2 supports and Pt/Ce catalysts with various metal promoters. (A) CeO_2 support and Pt/Ce catalyst; (B) Me/Pt/Ce catalysts; and (C) Me/Ce samples.

Metal doping in CeO_2 can lower the surface defect formation energy, leading to the generation of more labile oxygen species at the surface.[51,52] In the case of the Nb/Ce and W/Ce samples, the reduction peak moved to around 520 °C, and for the Al/Ce and Ga/Ce samples, reduction proceeded at a lower temperature of about 494 °C and 390 °C, respectively. However, the total reduction amount in all Me/CeO_2 samples was not significantly different from that of pure CeO_2. This observation indicates that the promoters primarily modulate the reduction behavior of the CeO_2 surface by enhancing the reducibility of surface oxygen, thereby facilitating its reduction at lower temperatures. Although Al and Ga promoters enhance the reducibility of surface oxygen, as reflected by the lower reduction temperatures in H_2-TPR, this increased reducibility does not directly translate into higher CO uptake. In conjunction with the pulsed CO-chemisorption results, these observations indicate that enhanced reducibility of the CeO_2 surface alone is not sufficient to promote CO adsorption.

The structural characteristics of the catalysts were analyzed using Raman spectroscopy, and the results are shown in Fig. 4. All CeO_2-based samples exhibited a strong peak at ~460 cm^{-1}, which corresponds to the F_{2g} mode of fluorite-type CeO_2.[13,47,53] This vibration arises from the symmetric stretching vibration of the oxygen octahedra (O–Ce–O) surrounding Ce^{4+}.[13,53] The F_{2g} band is regarded as a structure-sensitive indicator that reflects changes in the CeO_2 crystal, such as defect density, metal doping effects, or lattice distortion due to heat treatment.[54] The weak peak at 400 cm^{-1} corresponds to the O–Ce and Ce–O stretching vibration modes on the CeO_2 (111) surface, which are attributed to a surface structure with low symmetry.[55] As shown in Fig. 4(A), the Pt/Ce catalyst exhibited a decreased intensity and a shift of the F_{2g} peak to lower wavenumber values compared with the bare CeO_2 support. This indicates that Pt loading induces lattice distortion, leading to the formation of oxygen vacancies accompanied by the partial reduction of Ce^{4+} to Ce^{3+}.[54] These changes in the F_{2g} band imply that a fraction of Pt species is partially incorporated into CeO_2 surface lattice sites, which is consistent with the XRD results.[12,54] In addition, the CeO_2 support showed only a weak defect-induced D mode at 600 cm^{-1}, whereas the Pt/Ce catalyst presented two additional bands at ~560 and ~660 cm^{-1}. The peak at 600 cm^{-1} is a D mode of the CeO_2 lattice, associated with structural defects resulting from the substitution of Ce^{4+} ions with Ce^{3+} or other impurities.[53,55] For the Pt/Ce catalyst, the defect-induced D mode at ~600 cm^{-1} cannot be distinctly separated due to spectral overlap with Pt-related vibrational features. The 560 cm^{-1} peak is an asymmetric stretching vibration due to the Pt–O–Ce bond, reflecting MSI.[47,53,55] The band at 660 cm^{-1} corresponds to Pt–O vibrations from amorphous PtO_x species dispersed on the surface.[47,53,55]

Fig. 4(B) shows the Raman spectra of the calcined Me/Pt/Ce catalysts without pretreatment for the reaction. Compared with the undoped Pt/Ce catalyst, the Me/Pt/Ce catalyst exhibited a decrease in the intensities of peaks at 560 cm^{-1} (Pt–O–Ce) and 660 cm^{-1} (PtO_x). This decrease suggests that the promoter metals partially interact with Pt, resulting in interfacial reorganization of the Pt–O–Ce interfacial bonding and the Pt–O coordination environment. This interpretation is consistent with the H_2-TPR results, which showed a downshift in the reduction temperature upon the addition of promoters to the Pt/Ce catalyst. Fig. 4(C) presents the Raman spectra of the reduced Me/Pt/Ce catalysts after H_2-reduction pretreatment. The peaks at 560 cm^{-1} and 660 cm^{-1} observed in all calcined catalysts were attenuated, leaving a weak D mode at 600 cm^{-1}. This indicates that the PtO_x species was reduced to metallic Pt^0 during the H_2 pretreatment, with some distortion of the CeO_2 lattice remaining and the surface oxygen defect structure being maintained. Based on the H_2-TPR and pulsed CO-chemisorption results, these Raman observations suggest that the introduced promoters interact with both Pt species and the

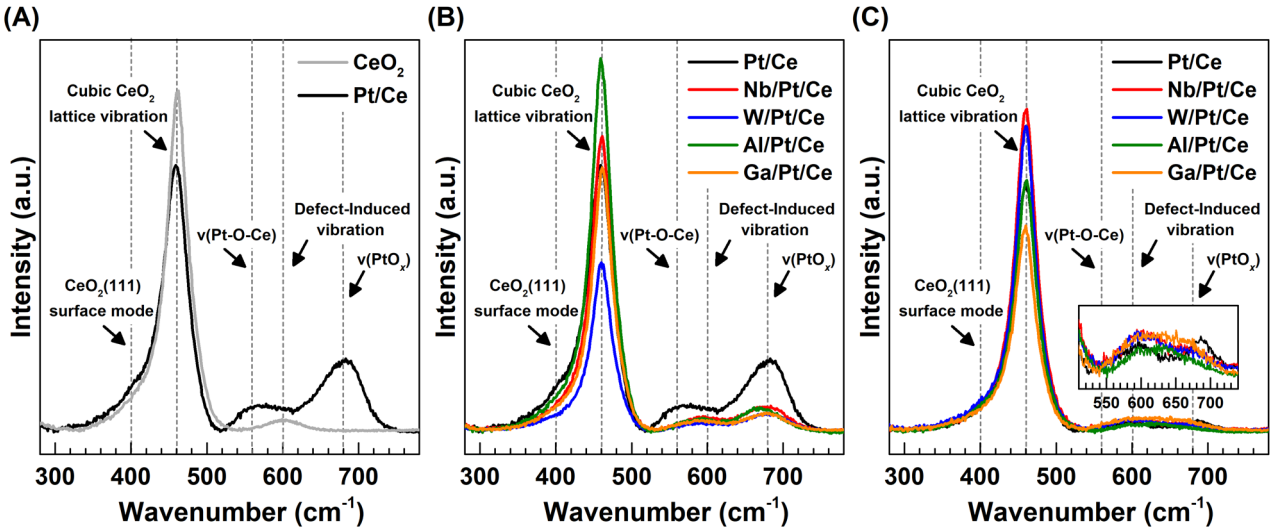

Fig. 4 Raman spectra of the CeO_2 support and Pt/Ce catalysts with various metal promoters. (A) Calcined CeO_2 support and Pt/Ce catalyst; (B) calcined Me/Pt/Ce catalysts; and (C) reduced Me/Pt/Ce catalysts.

CeO_2 support, leading to a modification of the original Pt–O–Ce interfacial structure.

3.3. Oxygen mobility and surface chemical states of Me/Pt/Ce catalysts

Fig. 5 integrates OSC-related values obtained from XPS (O 1s and Ce 3d) and H_2–O_2 pulse chemisorption analyses for Pt/Ce catalysts prepared with various promoters. In the WGS reaction, OSC plays a crucial role in enhancing catalytic activity at high temperatures through the redox pathway.[13,53,54] CO chemisorption on the active Pt sites constitutes an essential initial step, and, following the Mars-van Krevelen mechanism, CO adsorbed on Pt reacts with redox-active oxygen species at the Pt–CeO_2 interface to form CO_2, while surface oxygen vacancies are replenished by oxygen derived from H_2O dissociation, accompanied by H_2 formation.[12,56] Oxygen vacancies act as reservoirs for mobile lattice oxygen species, which can migrate from the CeO_2 support to interfacial Pt–CeO_2 sites and directly participate in the redox cycle.[10,12] In particular, these defect-derived mobile oxygen species not only accelerate the redox cycle of the WGS reaction but also play a crucial role in enhancing the sulfur tolerance of the catalyst. Previous studies have shown that sulfur species adsorbed on Pt active sites are oxidatively removed in the form of SO_2 by mobile oxygen originating from the CeO_2 support through oxygen reverse spillover, indicating that OSC has a positive influence on sulfur removal.[14,17–19] Fig. S6 presents the XPS spectra and corresponding deconvolutions of the Ce 3d and O 1s orbitals for the reduced catalysts. The Ce^{3+} species is generated by the loss of oxygen atoms from the lattice during the reduction of CeO_2; thus, its presence reflects the existence of mobile oxygen and oxygen vacancies within the catalyst.[13] As shown in Fig. S6(A), the Ce 3d spectra were deconvoluted into 10 peaks attributed to Ce^{3+} (v_0, v', u_0 and u') and Ce^{4+} (v, v'', v''', u, u'', and u''').[57,58] The peak labeled "u" corresponds to the $3d_{3/2}$ spin–orbit state, and the peak labeled "v" corresponds to the $3d_{5/2}$ state. The Ce^{3+} ratio calculated from the integrated peak areas increased upon promoter addition to the Pt/Ce catalyst (Fig. 5(A)). The increase was relatively larger in the W- and Ga-promoted catalysts compared to the other promoted catalysts. This enhancement can be attributed to changes induced by interactions between the promoter and Ce as well as Pt species on the catalyst surface. Similarly, defective oxygen species are closely associated with both mobile oxygen and oxygen vacancies, and can be used as an indicator of the oxygen storage and release capacity of the catalyst.[13,43] The O 1s spectra (Fig. S6(B)) comprise three oxygen species, corresponding to lattice oxygen (O_L, O^{2-}, ~529.4 eV), defective oxygen (O_D, O_2^{2-} or O^-, ~530.4 eV), and surface hydroxyl groups (O_A, ~531.5 eV).[43,48,57] Calculations based on peak area ratios (Fig. 5(B)) showed that the O_D ratio exhibited the same trend as the Ce^{3+} ratio.

To quantitatively evaluate the OSC of each catalyst, H_2–O_2 pulse chemisorption analysis was performed at the reaction temperature of 400 °C (Fig. 5(C)). The bare CeO_2 showed a low OSC value of 0.04×10^{-5} gmol g_{cat}^{-1}, whereas the Pt/Ce catalyst loaded with Pt increased significantly to 2.75×10^{-5} gmol g_{cat}^{-1}, indicating that Pt loading promotes oxygen exchange between Pt and the CeO_2 support, thereby enhancing the OSC of the catalyst. This is consistent with the H_2-TPR results, indicating that reverse oxygen spillover from the CeO_2 surface is induced by the formation of interfacial interactions between Pt and Ce upon Pt doping. In line with the XPS results, the addition of promoters to the Pt/Ce catalyst further enhanced the OSC of all Me/Pt/Ce catalysts ($3.28–4.84 \times 10^{-5}$ gmol g_{cat}^{-1}). The introduction of promoters can increase oxygen defect formation and OSC by inducing local lattice distortion arising from ionic radius differences and valence imbalance relative to Ce^{4+}, owing to the incorporation of dopant ions (Nb^{5+}, W^{6+}, Al^{3+}, and Ga^{3+}).[52,59,60] As for the XRD results, promoter metals with smaller ionic radii than Ce^{4+} are incorporated into the surface lattice of the catalyst. The W- and Ga-promoted catalysts exhibited relatively high OSC values among the Me/Pt/Ce catalysts. However, under sulfur-containing WGS reaction conditions, the catalytic behaviors of the Me/Pt/Ce catalysts differed markedly. In particular, the high OSC observed for the Ga/Pt/Ce catalyst did not directly translate into enhanced sulfur tolerance or improved catalytic regeneration.

Recent studies have reported that oxygen vacancies located at perimeter Pt–O–Ce sites play a decisive role in regulating adsorbate activation, water dissociation, and interfacial redox cycling.[61] Therefore, under continuous sulfur exposure, maintaining catalytic activity depends not only on a high OSC, but also on the ability of stored oxygen to actively participate in interfacial redox processes at Pt active sites. From this perspec-

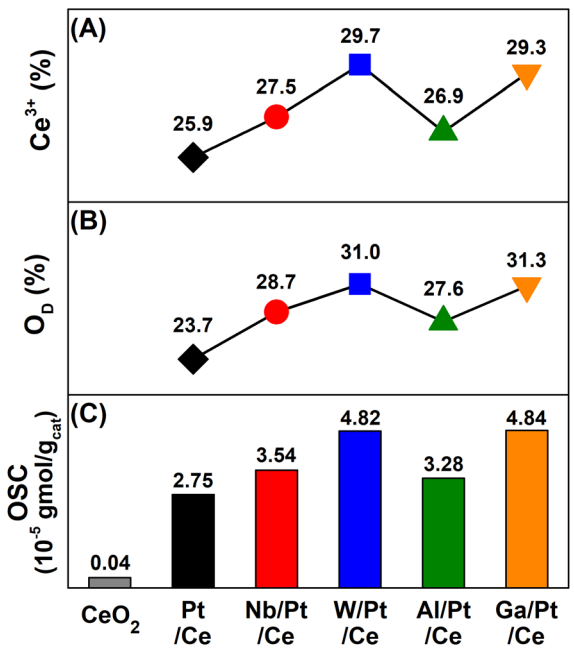

Fig. 5 Oxygen storage capacity-related values of the Pt/Ce catalysts with various metal promoters. (A) Ce^{3+} ratio calculated from XPS Ce 3d spectra; (B) O_D ratio calculated from XPS O 1s spectra; (C) OSC values obtained from H_2–O_2 pulse chemisorption.

tive, in the W-promoted catalyst, mobile oxygen species can be effectively delivered to Pt active sites through a preserved Pt–O–Ce interfacial structure, enabling oxidative sulfur removal. In contrast, although the Ga-promoted catalyst possesses a high density of oxygen defects, the weakened Pt–O–Ce interaction limits oxygen transfer to Pt active sites, resulting in diminished WGS activity and regeneration performance.

Fig. 6 shows the CO-DRIFTS spectra of Me/Pt/Ce catalysts recorded in the range of 2140–2000 cm^{-1} after CO chemisorption at 50 °C for 60 min following reduction pretreatment. The CO-DRIFTS spectra collected in the range of 1000–4000 cm^{-1} over 60 min at 10 min intervals are presented in Fig. S7. For all Me/Pt/Ce catalysts, two linear CO adsorption bands on metallic Pt^0 sites are observed at approximately 2090 and 2070 cm^{-1}, which are commonly assigned to well-coordinated and low-coordinated Pt sites, respectively.[47,62] In general, interfacial interactions between the metal and the support induce charge transfer, which modifies the electronic structure of metal active sites and thereby regulates CO adsorption strength. The intensity of the dominant band at ~2070 cm^{-1} is highest for the W/Pt/Ce catalyst, followed by the Nb/Pt/Ce, Al/Pt/Ce, and Ga/Pt/Ce catalysts, which is consistent with the trend observed in the CO-chemisorption results. Accordingly, the enhancement of the 2070 cm^{-1} band reflects an increased availability of Pt^0 sites for CO adsorption, while the extent of Pt–CeO_2 electronic interaction is inferred from the frequency shift of this band rather than from its intensity alone. In addition, a noticeable blue shift of the ~2070 cm^{-1} band is observed for the W/Pt/Ce catalyst compared to the Ga/Pt/Ce catalyst. This frequency shift can be attributed to enhanced electron transfer from Pt to the CeO_2 support, resulting in a relative decrease in the electron density of Pt and weakened π back-donation to the CO 2π* antibonding orbital. Transition metal promoters such as W^{6+} and Nb^{5+} preserve strong Pt–O–Ce interactions while modifying the electronic structure of Pt, which facilitates π back-donation to the CO molecule and results in enhanced CO adsorption. In contrast, nontransition metal promoters such as Al^{3+} and Ga^{3+}, despite increasing the overall concentration of oxygen vacancies, exhibit a weaker electronic interaction at the Pt–O–Ce interface, which is reflected in comparatively lower CO chemisorption compared to the unpromoted Pt/Ce catalyst. These observations suggest that W incorporation simultaneously strengthens the electronic interaction at the Pt–O–Ce interface. This interpretation is consistent with the H_2-TPR results and, when combined with the OSC data, suggests that Pt sites primarily function as the active sites for CO adsorption, whereas mobile oxygen species generated and transmitted through strong, electronically interactive Pt–O–Ce bonding act as the sulfur-tolerant active sites.

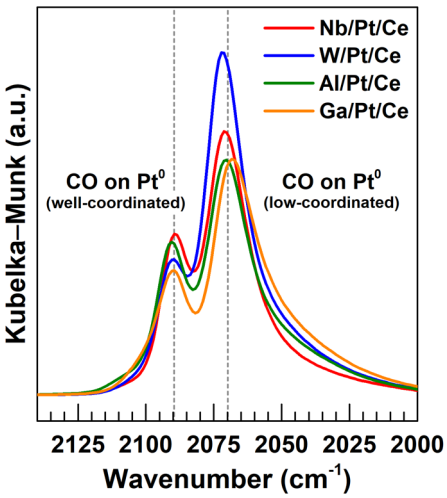

Fig. 6 CO-DRIFTS spectra recorded in the 2140–2000 cm^{-1} range at 50 °C after 60 min of CO adsorption on reduced Me/Pt/Ce catalysts with various metal promoters.

3.4. Discussion on sulfur tolerance and regeneration behavior of Nb- and W-promoted Pt/Ce catalysts

As confirmed in Fig. 1(B), the addition of transition metals significantly enhanced sulfur resistance and catalytic activity recovery of the Pt/Ce catalyst. The Nb/Pt/Ce and W/Pt/Ce catalysts exhibited comparable catalytic activities in the reaction test with 1000 ppm H_2S. Under harsher reaction conditions, with the H_2S concentration raised from 1000 to 1500 ppm, a test consisting of four sulfur on/off switching cycles was conducted for each catalyst to further examine the performance differences between the two catalysts (Fig. 7). These cycling tests were performed under repeatedly applied, harsh sulfur-poisoning conditions to evaluate the long-term stability of the two catalysts and to identify the factors influencing sulfur tolerance and activity regeneration behavior. Fig. 7(A) presents the time-on-stream profiles obtained during the sulfur on/off switching cycles, while Fig. 7(B) highlights the representative points from each cycle to facilitate comparison between the two catalysts. In these figures, empty symbols represent the sulfur-on state, whereas solid symbols indicate the sulfur-off state. In the first cycle, both catalysts maintained 50% CO conversion even under higher H_2S injection conditions, and the W/Pt/Ce catalyst showed slightly higher catalytic activity than the Nb/Pt/Ce catalyst. As the reaction proceeded to the second cycle, the W/Pt/Ce catalyst showed gradual catalytic deactivation along with a reduced activity regeneration rate compared with the Nb/Pt/Ce catalyst. From the third cycle onward, sulfur-induced catalytic deactivation of the W/Pt/Ce catalyst progressed more rapidly than in the preceding cycles, which was accompanied by a noticeable decline in catalytic activity recovery during the sulfur-off step. In the final cycle, the Nb/Pt/Ce catalyst maintained higher CO conversion, and the performance difference between the two catalysts became increasingly pronounced. A similar trend was observed in the sulfur-tolerance and long-term stability tests conducted under a constant H_2S flow of 1500 ppm for 30 h (Fig. S8). Under continuous sulfur-poisoning conditions, the difference in catalytic activity between the W/Pt/Ce and Nb/Pt/Ce catalysts increased with time compared with that observed in the cycling tests. This accelerated deactivation of the W/Pt/Ce catalyst was more

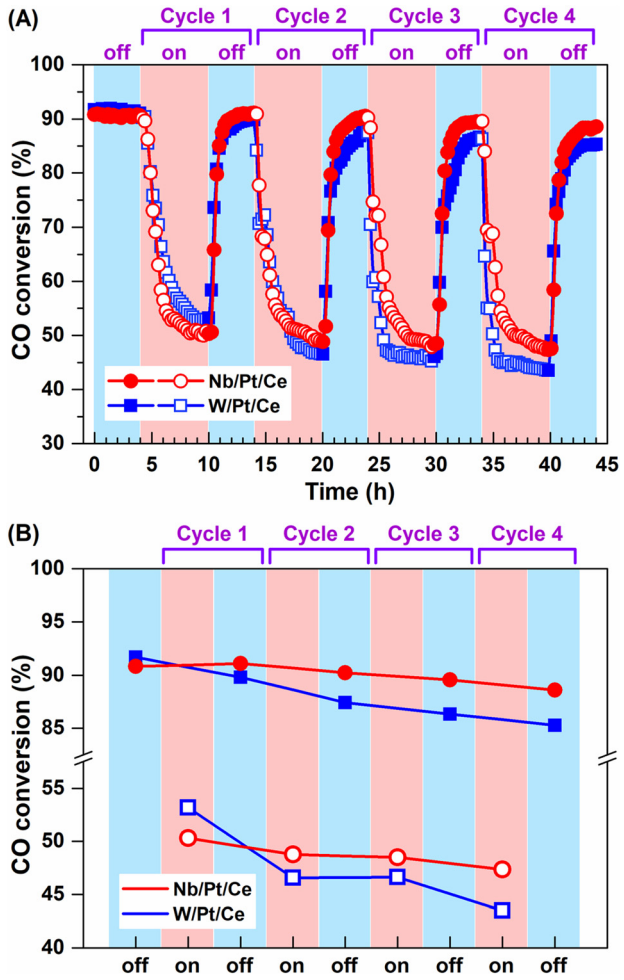

Fig. 7 Sulfur on/off switching cycling tests over Pt/Ce catalysts promoted with Nb and W. Reaction conditions: $H_2O/(CH_4 + CO + CO_2)$ = 2.0; T = 400 °C; GHSV = 46 000 mL g^{-1} h^{-1}; H_2S = 1500 ppm. (A) Time-on stream profiles; and (B) comparison of representative points for each cycle.

clearly observed under sustained H_2S exposure without regeneration, owing to its relatively lower sulfur resistance.

Overall, these results reaffirm that the metal–support interfacial structure and OSC are essential factors governing sulfur tolerance and catalytic activity regeneration of the Pt/Ce catalyst. Concurrently, the results suggest that the intrinsic chemical properties of the introduced promoter metals should be considered. Compared with the Nb/Pt/Ce catalyst, the W/Pt/Ce catalyst exhibits higher initial sulfur resistance and regeneration catalytic performance, which can be attributed to its superior CO adsorption capability, stronger Pt–O–Ce interfacial interaction, and enhanced oxygen mobility. This behavior suggests that W plays a beneficial role in strengthening the interfacial redox functionality. However, to more clearly understand the long-term stability differences, the distinct sulfidation behaviors of W and Nb under the H_2O-rich WGS reaction conditions in the presence of H_2S must be considered. Niobium exhibits a strong affinity for oxygen and preferentially forms highly stable oxides, such as Nb_2O_5 and NbO_2, with formation enthalpies of −380 and −395 kJ mol^{-1}, respectively, which are more negative than that of WO_3 (−279 kJ mol^{-1}).[63,64] This indicates that Nb–O bonding is thermodynamically more stable than W–O bonding. Furthermore, the Gibbs free energy changes for the sulfidation of Nb oxides by H_2S at 600 K are positive (+82 kJ mol^{-1} for NbO_2 and +108 kJ mol^{-1} for Nb_2O_5).[65] Therefore, under H_2O-rich WGS reaction conditions, Nb oxides are expected to resist transformation into sulfide phases. In contrast, the sulfidation of WO_3 exhibits a negative Gibbs free energy (−110 kJ mol^{-1}), indicating that the formation of W–S species is thermodynamically favorable.[65] These results suggest that Nb-based catalysts possess an inherently higher resistance to sulfur-induced transformation, whereas metals with negative sulfidation free energy are more prone to sulfur accumulation and potential deactivation.[63,65,66] Consequently, despite its superior initial catalytic performance, the W/Pt/Ce catalyst suffers from inferior long-term stability compared with the Nb/Pt/Ce catalyst. In contrast, the Nb/Pt/Ce catalyst maintains a more stable Pt–O–Ce interfacial structure, while suppressing thermodynamically unfavorable sulfidation, which is likely responsible for its enhanced long-term sulfur tolerance and catalytic activity regeneration. Table S1 provides a comparison of reported data on CO conversion or turnover frequency values for the WGS reaction using sulfur-tolerant catalysts. The optimized Nb/Pt/Ce catalyst developed in this study exhibits superior catalytic activity, even under conditions of relatively high GHSV and elevated sulfur concentrations. To assess long-term catalytic activity and durability for actual operations, the evaluations were conducted under harsh conditions. These included a simulated waste-derived synthesis gas reflecting real industrial environments and an applied GHSV of 46 000 h^{-1}, which is more than ten times higher than typical commercial WGS processes (~4000 h^{-1}).[2] Ultimately, the excellent performance of the developed catalyst suggests that the developed catalyst has strong potential for application in WGS processes within waste-to-hydrogen systems.

4. Conclusions

Herein, Pt/CeO_2 catalysts promoted by transition (Nb, W) and nontransition metals (Al, Ga) were applied to the WGS reaction under syngas conditions derived from sulfur-containing waste, and their sulfur tolerance, regeneration ability, long-term stability, and structural properties were systematically compared. The introduction of promoters induced reorganization of the Pt–O–Ce interface through interactions between the active metal and the support, which significantly altered the CO adsorption capacity, Pt–Ce bond strength, and oxygen mobility. The results of this study demonstrate that sulfur tolerance in Pt/CeO_2-based WGS catalysts is governed not solely by the concentrations of OSC, but more critically by the stability and functionality of the Pt–O–Ce interfacial structure. The Al- and Ga-promoted Pt/Ce catalysts exhibited enhanced OSC

relative to unpromoted Pt/Ce catalysts yet inferior sulfur resistance, indicating that excessive weakening of the Pt–Ce interaction limits the ability of activated oxygen species to participate in continuous sulfur oxidation and removal. In contrast, transition metal promoters that preserve a robust interfacial configuration enable sustained regeneration of Pt active sites under sulfur exposure, as observed for Nb- and W-promoted systems. Building on these insights, the design of sulfur-tolerant WGS catalysts should maintain a stable Pt–Ce interface capable of sustaining mobile and reactive oxygen species, rather than improving OSC alone. This interfacial design strategy is expected to extend catalyst lifetime, reduce performance losses associated with sulfur poisoning, and improve the operational reliability of the WGS reaction in waste-to-hydrogen conversion processes, thereby providing practical guidance for the rational design of sulfur-resistant WGS catalysts.

Author contributions

Ga-Ram Hong: conceptualization, data curation, formal analysis, investigation, methodology, visualization, and writing – original draft. Kyoung-Jin Kim: data curation, formal analysis, methodology, and visualization. Bong-Gyeong Shin: data curation, formal analysis, methodology, and visualization. Hyun-Seog Roh: supervision, funding acquisition, and writing – review and editing.

Conflicts of interest

There are no conflicts to declare.

Data availability

The data supporting the findings of this study are available in the article and its supplementary information (SI). Supplementary information: catalyst characterization methods, the results of the catalytic evaluation, adsorption–desorption curves, XPS spectra, and CO-DRIFTS spectra. See DOI: https://doi.org/10.1039/d6gc00981f.

Acknowledgements

This study was supported by a National Research Foundation of Korea (NRF) grant funded by the Korean government (MSIT) (No. 2023R1A2C2007671).

References

1 S. Y. Ahn, K. J. Kim, B. J. Kim, G. R. Hong, W. J. Jang, J. W. Bae, Y. K. Park, B. H. Jeon and H. S. Roh, *Renew. Sustain. Energy Rev.*, 2023, **186**, 113635, DOI: 10.1016/j.rser.2023.113635.
2 Y. L. Lee, K. J. Kim, G. R. Hong and H. S. Roh, *Chem. Eng. J.*, 2023, **458**, 141422, DOI: 10.1016/j.cej.2023.141422.
3 J. Lui, W. H. Chen, D. C. W. Tsang and S. You, *Renew. Sustain. Energy Rev.*, 2020, **134**, 110365, DOI: 10.1016/j.rser.2020.110365.
4 L. Makarichi, W. Jutidamrongphan and K.-a. Techato, *Renew. Sustain. Energy Rev.*, 2018, **91**, 812–821, DOI: 10.1016/j.rser.2018.04.088.
5 S. C. Wijayasekera, K. Hewage, O. Siddiqui, P. Hettiaratchi and R. Sadiq, *Int. J. Hydrogen Energy*, 2022, **47**, 5842–5870, DOI: 10.1016/j.ijhydene.2021.11.226.
6 M. Sajid, A. Raheem, N. Ullah, M. Asim, M. S. U. Rehman and N. Ali, *Renew. Sustain. Energy Rev.*, 2022, **168**, 112815, DOI: 10.1016/j.rser.2022.112815.
7 Y. L. Lee, K. Lee, C. H. Ko and H. S. Roh, *Chem. Eng. J.*, 2022, **431**, 134299, DOI: 10.1016/j.cej.2021.134299.
8 W. J. Jang, J. O. Shim, K. W. Jeon, H. S. Na, H. M. Kim, Y. L. Lee, H. S. Roh and D. W. Jeong, *Appl. Catal. B: Environ.*, 2019, **249**, 72–81, DOI: 10.1016/j.apcatb.2019.02.036.
9 A. Saravanakumar, W. H. Chen, K. D. Arunachalam, Y. K. Park and H. C. Ong, *Fuel*, 2022, **315**, 123287, DOI: 10.1016/j.fuel.2022.123287.
10 E. Lee, S. Kang, A. Beck, J. Park, J. Lee and D. H. Kim, *ACS Catal.*, 2025, **15**, 9477–9488, DOI: 10.1021/acscatal.5c01564.
11 J. Zhang, X. Qin, X. Chu, M. Chen, X. Chen, J. Chen, H. He and C. Zhang, *Environ. Sci. Technol.*, 2021, **55**, 16687–16698, DOI: 10.1021/acs.est.1c06400.
12 Z. Shui, F. Zhang, H. Yang, M. Zhao, Z. Zhao, G. Li, Z. Wei, G. Jiang, Z. Zhang and Z. Hao, *Adv. Funct. Mater.*, 2025, **35**, 2415774, DOI: 10.1002/adfm.202415774.
13 S. Y. Ahn, W. J. Jang, J. O. Shim, B. H. Jeon and H. S. Roh, *Catal. Rev. Sci. Eng.*, 2024, **66**, 1316–1399, DOI: 10.1080/01614940.2022.2162677.
14 Y. L. Lee, K. J. Kim, G. R. Hong, S. Y. Ahn, B. J. Kim, J. O. Shim and H. S. Roh, *Renew. Energy*, 2021, **178**, 334–343, DOI: 10.1016/j.renene.2021.06.084.
15 Y. L. Lee, K. J. Kim, G. R. Hong, S. Y. Ahn, B. J. Kim, H. R. Park, S. J. Yun, J. W. Bae, B. H. Jeon and H. S. Roh, *ACS Sustainable Chem. Eng.*, 2021, **9**, 15287–15293, DOI: 10.1021/acssuschemeng.1c05456.
16 G. R. Hong, K. J. Kim, S. Y. Ahn, B. J. Kim, H. R. Park, Y. L. Lee, S. S. Lee, Y. Jeon and H. S. Roh, *Catalysts*, 2022, **12**, 1670, DOI: 10.3390/catal12121670.
17 K. J. Kim, G. R. Hong, S. Y. Ahn, B. J. Kim, Y. L. Lee and H. S. Roh, *Catal. Today*, 2024, **425**, 114336, DOI: 10.1016/j.cattod.2023.114336.
18 G. R. Hong, K. J. Kim, S. Y. Ahn, B. J. Kim, B. G. Shin, M. J. Oh, Y. L. Lee and H. S. Roh, *Catalysts*, 2024, **14**, 99, DOI: 10.3390/catal14020099.
19 G. R. Hong, B. G. Shin, K. J. Kim, Y. L. Lee, E. Y. Ju and H. S. Roh, *Catal. Today*, 2026, **461**, 115513, DOI: 10.1016/j.cattod.2025.115513.
20 X. Zou, Y. Meng, J. Liu, Y. Cao, L. Cui, Z. Shen, Q. Xia, X. Li, S. Zhang, Z. Ge, Y. Pan and Y. Wang, *Inorg. Chem.*, 2024, **63**, 881–890, DOI: 10.1021/acs.inorgchem.3c03881.

21 C. H. Jeong, K. W. Jeon, H. J. Byeon, T. Y. Choi, H. M. Kim and D. W. Jeong, *J. Ind. Eng. Chem.*, 2021, **100**, 149–158, DOI: 10.1016/j.jiec.2021.05.027.
22 C. Sener, T. S. Wesley, A. C. Alba-Rubio, M. D. Kumbhalkar, S. H. Hakim, F. H. Ribeiro, J. T. Miller and J. A. Dumesic, *ACS Catal.*, 2016, **6**, 1334–1344, DOI: 10.1021/acscatal.5b02028.
23 M. Wang, Z. Tian, R. Nie, Q. Zhong, J. Cao, M. Wang, J. Chen and Q. Zhang, *Sep. Purif. Technol.*, 2024, **350**, 127923, DOI: 10.1016/j.seppur.2024.127923.
24 V. Palma, F. Gallucci, P. Pullumbi, C. Ruocco, E. Meloni and M. Martino, *Catalysts*, 2020, **10**, 564, DOI: 10.3390/catal10050564.
25 K. G. Azzam, I. V. Babich, K. Seshan, B. L. Mojet and L. Lefferts, *ChemCatChem*, 2013, **5**, 557–564, DOI: 10.1002/cctc.201200492.
26 M. F. Tonekaboni, M. Rezaei, S. M. Alavi and E. Akbari, *Int. J. Hydrog. Energy*, 2025, **101**, 139–147, DOI: 10.1016/j.ijhydene.2024.12.352.
27 J. Vecchietti, A. Bonivardi, W. Xu, D. Stacchiola, J. J. Delgado, M. Calatayud and S. E. Collins, *ACS Catal.*, 2014, **4**, 2088–2096, DOI: 10.1021/cs500323u.
28 J. Zhou, Y. Du, Y. Qiao, F. Zhou, Z. Liu, Z. Xiong, M. Liu and W. Lu, *J. Environ. Chem. Eng.*, 2025, **13**, 116666, DOI: 10.1016/j.jece.2025.116666.
29 Y. Wang, J. Wang, Y. Zhang, Q. Guo, J. An, Y. Liang, Y. Wang, P. Cao, M. Heggen, R. E. Dunin-Borkowski, X. Zhu, X. Li and F. Wang, *ChemCatChem*, 2022, **14**, e202200982, DOI: 10.1002/cctc.202200982.
30 D. Zhou, Z. Li, Y. Deng, C. Dang and W. Cai, *Fuel*, 2024, **357**, 129851, DOI: 10.1016/j.fuel.2023.129851.
31 Y. Nakaya, J. Hirayama, S. Yamazoe, K.-i. Shimizu and S. Furukawa, *Nat. Commun.*, 2020, **11**, 2838, DOI: 10.1038/s41467-020-16693-9.
32 D. W. Jeong, W. J. Jang, J. O. Shim, W. B. Han, K. W. Jeon, Y. C. Seo, H. S. Roh, J. H. Gu and Y. T. Lim, *J. Mater. Cycles Waste Manage.*, 2014, **16**, 650–656, DOI: 10.1007/s10163-014-0272-8.
33 C. Hulteberg, *Int. J. Hydrog. Energy*, 2012, **37**, 3978–3992, DOI: 10.1016/j.ijhydene.2011.12.001.
34 O. Kröcher, M. Widmer, M. Elsener and D. Rothe, *Ind. Eng. Chem. Res.*, 2009, **48**, 9847–9857, DOI: 10.1021/ie900882p.
35 I. Mochida, S. Miyamoto, K. Kuroda, S. Kawano, S. Yatsunami, Y. Korai, A. Yasutake and M. Yoshikawa, *Energy Fuels*, 1999, **13**, 369–373, DOI: 10.1021/ef980070f.
36 R. D. Shannon, *Acta Crystallogr. Sect. A*, 1976, **32**, 751–767, DOI: 10.1107/S0567739476001551.
37 W. Tan, S. Xie, D. Le, W. Diao, M. Wang, K. B. Low, D. Austin, S. Hong, F. Gao, L. Dong, L. Ma, S. N. Ehrlich, T. S. Rahman and F. Liu, *Nat. Commun.*, 2022, **13**, 7070, DOI: 10.1038/s41467-022-34797-2.
38 B.-Y. Wu, Z.-S. Huang, D.-F. Zhao, F.-J. Hu, B.-X. Peng, N. Pu, S.-G. Zhang and X.-B. Huang, *Rare Met.*, 2025, **44**, 6303–6318, DOI: 10.1007/s12598-025-03402-y.
39 L. Long, S. Tian, Y. Zhao, X. Zhang, W. Luo and X. Yao, *J. Colloid Interface Sci.*, 2023, **648**, 876–888, DOI: 10.1016/j.jcis.2023.06.020.
40 L. Wang, M. Al-Mamun, Y. L. Zhong, L. Jiang, P. Liu, Y. Wang, H. G. Yang and H. Zhao, *Sustainable Energy Fuels*, 2017, **1**, 1013–1017, DOI: 10.1039/C6SE00097E.
41 M. Thommes, K. Kaneko, A. V. Neimark, J. P. Olivier, F. Rodriguez-Reinoso, J. Rouquerol and K. S. W. Sing, *Pure Appl. Chem.*, 2015, **87**, 1051–1069, DOI: 10.1515/pac-2014-1117.
42 T. Tanabe, Y. Nagai, T. Hirabayashi, N. Takagi, K. Dohmae, N. Takahashi, S. Matsumoto, H. Shinjoh, J. N. Kondo, J. C. Schouten and H. H. Brongersma, *Appl. Catal. A: Gen.*, 2009, **370**, 108–113, DOI: 10.1016/j.apcata.2009.09.030.
43 L. Du, A. Li, S. Hu, S. Su, Y. Wang, L. Jiang, J. Xu, K. Xu and J. Xiang, *Prog. Solid State Chem.*, 2025, **78**, 100520, DOI: 10.1016/j.progsolidstchem.2025.100520.
44 A. Holmgren, B. Andersson and D. Duprez, *Appl. Catal. B: Environ.*, 1999, **22**, 215–230, DOI: 10.1016/S0926-3373(99)00047-8.
45 A. R. Puigdollers, P. Schlexer, S. Tosoni and G. Pacchioni, *ACS Catal.*, 2017, **7**, 6493–6513, DOI: 10.1021/acscatal.7b01913.
46 J. Lee, Y. Ryou, X. Chan, T. J. Kim and D. H. Kim, *J. Phys. Chem. C*, 2016, **120**, 25870–25879, DOI: 10.1021/acs.jpcc.6b08656.
47 M. Wang, Y. Zhang, Z. Wu, Y. Zheng, Z. Zhou and W. Weng, *Chem. Eng. J.*, 2022, **450**, 138171, DOI: 10.1016/j.cej.2022.138171.
48 J. Yu, X. Qin, Y. Yang, M. Lv, P. Yin, L. Wang, Z. Ren, B. Song, Q. Li, L. Zheng, S. Hong, X. Xing, D. Ma, M. Wei and X. Duan, *J. Am. Chem. Soc.*, 2024, **146**, 1071–1080, DOI: 10.1021/jacs.3c12061.
49 A. I. Stadnichenko, E. M. Slavinskaya, O. A. Stonkus and A. I. Boronin, *ChemCatChem*, 2024, **16**, e202301727, DOI: 10.1002/cctc.202301727.
50 M. Xiao, D. Han, X. Yang, J. Yu, B. Shi, Y. Guo, X. Yu and M. Ge, *Environ. Sci. Technol.*, 2024, **58**, 22808–22817, DOI: 10.1021/acs.est.4c06977.
51 J. Paier, C. Penschke and J. Sauer, *Chem. Rev.*, 2013, **113**, 3949–3985, DOI: 10.1021/cr3004949.
52 E. W. McFarland and H. Metiu, *Chem. Rev.*, 2013, **113**, 4391–4427, DOI: 10.1021/cr300418s.
53 T. A. Bugrova, T. S. Kharlamova, V. A. Svetlichnyi, A. S. Savel'eva, M. A. Salaev and G. V. Mamontov, *Catal. Today*, 2021, **375**, 36–47, DOI: 10.1016/j.cattod.2020.04.039.
54 R. Schmitt, A. Nenning, O. Kraynis, R. Korobko, A. I. Frenkel, I. Lubomirsky, S. M. Haile and J. L. M. Rupp, *Chem. Soc. Rev.*, 2020, **49**, 554–592, DOI: 10.1039/c9cs00588a.
55 C. Molinet-Chinaglia, E. Vera, P. Vernoux, L. Piccolo and S. Loridant, *Catal. Sci. Technol.*, 2024, **14**, 6247–6258, DOI: 10.1039/d4cy00741g.
56 X. I. Pereira-Hernández, A. DeLaRiva, V. Muravev, D. Kunwar, H. Xiong, B. Sudduth, M. Engelhard, L. Kovarik, E. J. M. Hensen, Y. Wang and A. K. Datye, *Nat. Commun.*, 2019, **10**, 1358, DOI: 10.1038/s41467-019-09308-5.
57 X. Chen, C. Qu, Y. Xiao, W. Wang, J. Zhang, X. Zheng and Q. Ye, *Catal. Today*, 2024, **434**, 114687, DOI: 10.1016/j.cattod.2024.114687.

58 R. Peng, S. Li, X. Sun, Q. Ren, L. Chen, M. Fu, J. Wu and D. Ye, *Appl. Catal. B: Environ*, 2018, **220**, 462–470, DOI: 10.1016/j.apcatb.2017.07.048.
59 K. C. Petallidou, K. Polychronopoulou, S. Boghosian, S. Garcia-Rodriguez and A. M. Efstathiou, *J. Phys. Chem. C*, 2013, **117**, 25467–25477, DOI: 10.1021/jp406059h.
60 X. Lin, C. Chen, J. Ma, X. Fang, Y. Zhan and Q. Zheng, *Int. J. Hydrog. Energy*, 2013, **38**, 11847–11852, DOI: 10.1016/j.ijhydene.2013.07.001.
61 Y. Li, M. Kottwitz, J. L. Vincent, M. J. Enright, Z. Liu, L. Zhang, J. Huang, S. D. Senanayake, W. C. D. Yang, P. A. Crozier, R. G. Nuzzo and A. I. Frenkel, *Nat. Commun.*, 2021, **12**, 914, DOI: 10.1038/s41467-021-21132-4.
62 H. Choi, S. Oh and J. Y. Park, *Catal. Today*, 2020, **352**, 212–219, DOI: 10.1016/j.cattod.2019.11.005.
63 J. K. Dash, L. Chen, P. H. Dinolfo, T. M. Lu and G. C. Wang, *J. Phys. Chem. C*, 2015, **119**, 19763–19771, DOI: 10.1021/acs.jpcc.5b04057.
64 L. Backman and E. J. Opila, *J. Eur. Ceram. Soc.*, 2019, **39**, 1796–1802, DOI: 10.1016/j.jeurceramsoc.2018.11.004.
65 M. Zdražil, *Catal. Today*, 1988, **3**, 269–365, DOI: 10.1016/0920-5861(88)87051-2.
66 H. Simchi, T. N. Walter, T. H. Choudhury, L. Y. Kirkley, J. M. Redwing and S. E. Mohney, *J. Mater. Sci.*, 2017, **52**, 10127–10139, DOI: 10.1007/s10853-017-1228-x.